INTERNATIONAL JOURNAL FOR NUMERICAL METHODS IN FLUIDS
Int. J. Numer. Meth. Fluids 2007; **53**:895–914
Published online 23 August 2006 in Wiley InterScience (www.interscience.wiley.com). DOI: 10.1002/fld.1309

Unsteady simulations of the flow around a short surface-mounted cylinder

R. J. Pattenden, N. W. Bressloff*,†, S. R. Turnock and X. Zhang

School of Engineering Sciences, University of Southampton, Highfield, Southampton, SO17 1BJ, U.K.

SUMMARY

The flow around a surface-mounted circular cylinder, of height/diameter ratio 1 with a free end, is simulated using large-eddy simulation (LES) and detached-eddy simulation (DES) at a Reynolds number based on diameter of 200 000. A comparison is made between the abilities of the two models to capture flow features observed in particle image velocimetry (PIV) experiments carried out by the authors. The flow contains three interacting features formed from the junction flow between the cylinder and the ground, separation from the cylinder wall and resultant turbulent wake, and the flow over the free-end of the cylinder. Both LES and DES overpredict the length of the recirculation region by 30%, but the turbulence quantities are close to the measured values. The topology of the flow over the free-end is confirmed as consisting of an arch or 'mushroom' vortex. Due to the high Reynolds number the grid resolution is insufficient to resolve the approaching ground-plane boundary layer flow with LES, leading to inaccuracies in the horseshoe vortex system. The DES model improves this area, though still has grid induced separation effects. Copyright © 2006 John Wiley & Sons, Ltd.

Received 2 September 2005; Revised 14 June 2006; Accepted 19 June 2006

KEY WORDS: large-eddy simulation; detached-eddy simulation; finite cylinder

1. INTRODUCTION

The bluff body considered is a low aspect ratio circular cylinder ($h/d = 1$ where h and d are the height and diameter, respectively) mounted on a ground plane, with an approaching turbulent boundary layer of thickness $0.1d$. The main features of this flow are shown in Figure 1. This flow has been examined experimentally by Pattenden *et al.* [1, 2]. Wind tunnel measurements were made of the flow including particle image velocimetry (PIV), surface flow visualization, hot-wire

*Correspondence to: N. W. Bressloff, School of Engineering Sciences, University of Southampton, Highfield, Southampton, SO17 1BJ, U.K.
†E-mail: nwb@soton.ac.uk

Contract/grant sponsor: University of Southampton

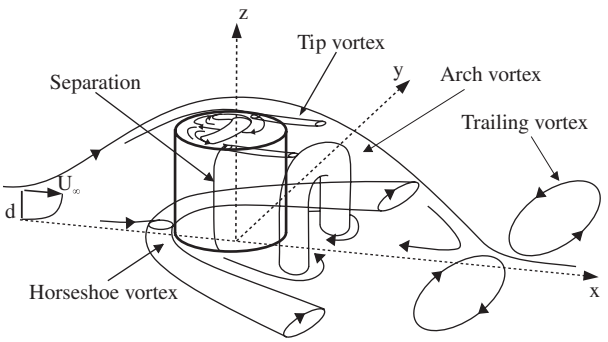

Figure 1. Schematic diagram of flow over truncated cylinder (not to scale).

anemometry in the wake and surface pressure measurements. In the time-averaged flow there are a number of three-dimensional vortex structures which define the topology of the flow. At the junction of the cylinder and the ground plane there is a turbulent horseshoe vortex system with one primary vortex but also two smaller vortices very close to the ground which are barely visible in the PIV measurements. This corresponds to the topology proposed by Baker [3]. On the free-end of the cylinder the mean flow exhibits a complex pattern but appears to consist principally of an arch vortex which loops over the free-end with its bases attached to the surface of the free-end. In the wake the mean flow is an arch vortex just behind the cylinder, with streamwise vortices trailing off the tip. Further downstream there are just two large streamwise vortices formed from the vorticity in the detached shear layer. Whilst the oncoming flow has a low level (0.3%) of background turbulence, the instantaneous flow is highly turbulent in the wake with weak periodicity in the vortex shedding.

The purpose of the numerical work presented here is to assess the applicability of current simulation methods to the type of complex flow that was found in the experiment. A Reynolds number of 200 000 (based on cylinder diameter) was chosen after initial tests had indicated that this was a suitably high value that captured all the flow features of interest whilst not demanding too high a flow speed for the wind tunnel or spatial and temporal resolutions for the CFD.

Earlier work using the k–ε model applied to the same geometry has shown poor performance of this Reynolds averaged turbulence model [2, 4]. As a result, the current work aims (i) to investigate the capability of large-eddy simulation (LES) and detached-eddy simulation (DES) to better predict the turbulent, three-dimensional separation region behind the truncated cylinder and the other associated flow features and (ii) to assess these capabilities without using excessively large computational resources.

One other set of LES of the flow around a finite-height cylinder has been published by Fröhlich *et al.* [5]. They performed LES at a Reynolds number of 43 000 and $h/d = 2.5$, corresponding to experiments carried out by Kappler [6]. They showed the presence of an arch vortex and tip vortices in the mean flow. They also found that on the 6 million cell grid that they used, the dynamic subgrid model gives too short a recirculation region.

Calculations of the flow past circular cylinders using DES have been performed by Travin *et al.* [7]. The principle purpose of these tests was to validate the model for flows with smooth-surface separation, which impose an additional challenge to turbulence models. Simulations were

DOI: 10.1002/fld

carried out with both laminar and turbulent separation, at Reynolds numbers from 5×10^4 to 3×10^6. Most of the simulations were performed using three-dimensional grids with a z-dimension of $2d$. The purely two-dimensional simulations gave markedly worse results. The comparisons with experimental data are not particularly favourable, partly due to differences in the Reynolds numbers and other conditions, and also due to the discrepancies between different sets of experiments. The drag and pressure coefficients differ from the experiment by about 20%, while the length of the recirculation region is overpredicted. The Reynolds stresses are close to the experimental values.

2. NUMERICAL METHOD

The flow solver [8] uses the finite volume method for discretizing the equations. It is based on structured multi-block grids using a collocated variable arrangement. The convective fluxes are discretized in space using the second order, curved line advection method (CLAM) [9] which is a member of the high resolution TVD scheme family. Although it is possible for this scheme to reduce to an upwind scheme in regions of high gradient, for example in shear layers, investigations have shown that this is generally not the case and v_t always dominates. The diffusive fluxes are discretized using second-order central differences. The SIMPLEC pressure-correction scheme is used, and the matrices are solved using the strongly implicit procedure (SIP). A second-order, implicit three time level method is used for the discretization in time.

In the LES method the incompressible Navier–Stokes equations are solved with an eddy viscosity based subgrid model. The model used is the structure-function model [10] where

$$\mu_t = 0.105 \rho C_K^{-3/2} \Delta x F_2^{1/2} \tag{1}$$

with

$$F_2 = \langle \| \overline{U}(\mathbf{x}, t) - \overline{U}(\mathbf{x} + \mathbf{r}, t) \|^2 \rangle_{\|\mathbf{r}\| = \Delta x}$$

Here C_K is the Kolmogorov constant and Δx is the cell size. This model has been shown to be less dissipative in isotropic flows than the commonly used Smagorinsky model. In this situation the inertial range is better predicted. In shear flows however it may be more dissipative than other models, which may make this model less suitable for some regions of the flow considered here [11].

DES is a method proposed by Spalart [12], in order to overcome the considerable computational cost involved with full LES. The basis of this method is that RANS models are quite capable of modelling boundary layer flows, but generally fail to predict the larger scale eddies in regions of separated flow. In these regions LES should be far better at capturing the flow physics. DES is therefore a hybrid of RANS and LES, where the model operates in RANS mode close to the walls and in LES mode away from the walls. The model used in these simulations is the original DES method of Spalart and is based on the Spalart–Allmaras (S–A) one equation turbulence model [13] which is defined as follows:

$$\frac{D\tilde{\nu}}{Dt} = c_{b1} \tilde{S} \tilde{\nu} + \frac{1}{\sigma} [\nabla \cdot ((\nu + \tilde{\nu}) \nabla \tilde{\nu}) + c_{b2} (\nabla \tilde{\nu})^2] - c_{w1} f_w \left[\frac{\tilde{\nu}}{l_{SA}} \right]^2 \tag{2}$$

DOI: 10.1002/fld

where

$$\tilde{\nu} = \frac{\nu_t}{f_{v1}}, \quad f_{v1} = \frac{\chi^3}{\chi^3 + c_{v1}^3}, \quad \chi = \frac{\tilde{\nu}}{\nu}$$
$$\tilde{S} \equiv S + \frac{\tilde{\nu}}{\kappa^2 l_{\mathrm{SA}}^2}\left(1 - \frac{\chi}{1 + \chi f_{v1}}\right) \tag{3}$$

$$f_w = g\left[\frac{1 + c_{w3}^6}{g^6 + c_{w3}^6}\right]^{1/6}$$
$$g = r + c_{w2}(r^6 - r), \quad r \equiv \frac{\tilde{\nu}}{\tilde{S}\kappa^2 l_{\mathrm{SA}}^2} \tag{4}$$

In the above S is the magnitude of vorticity and l_{SA} is the distance to the nearest wall. In the DES implementation the length scale is modified such that it depends on the cell spacing, Δ, far from the wall, while remaining equal to the wall distance close to the wall.

$$\tilde{l}_{\mathrm{SA}} \equiv \min(l_{\mathrm{SA}}, C_{\mathrm{DES}}\Delta) \tag{5}$$

where Δ is the largest dimension of the cell, not the cube root of their sum,

$$\Delta \equiv \max(\Delta x, \Delta y, \Delta z) \tag{6}$$

C_{DES} is a constant which defines the transition point between the DES and RANS modes. In isotropic turbulence it has been calibrated to $C_{\mathrm{DES}} = 0.65$. This has also been found to be suitable for most other flows [14] and is the value used here.

The computational domain was designed to replicate the flow conditions in the wind tunnel. Thus the dimensions of the domain matched the tunnel dimensions so that the blockage effects were the same. The length of the ground plane upstream of the cylinder was also the same, so that the effect of the ground plane boundary layer development was included.

The dimensions of the domain are shown in Figure 2. The domain size was $4.0d$ upstream of the cylinder, $6.7d$ downstream, $6.0d$ laterally and $4.0d$ vertically. The downstream length of the

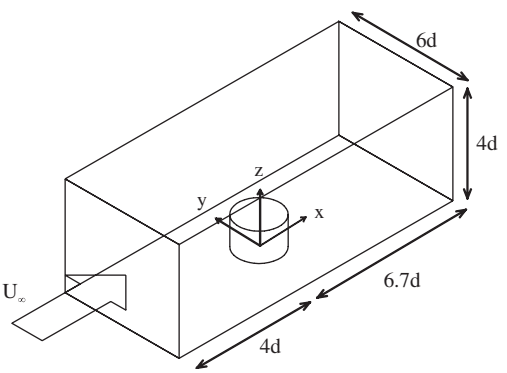

Figure 2. Dimensions of the computational domain.

DOI: 10.1002/fld

domain was felt to be sufficient, however it is a compromise between accuracy and computational cost and there may be some reflections from the boundary. No-slip conditions were applied to the walls of the tunnel, although the grid was not fine enough on the side and top walls to resolve the boundary layers on these surfaces. The effect of the lack of mesh in the top and side wall boundary layers was considered to be negligible. A uniform velocity was applied to the inlet and a zero-gradient condition to the outlet. The inlet of the domain was positioned at the start of the ground plate in the wind tunnel, where there was no boundary layer. Turbulence quantities were not set at the inlet due to difficulties associated with selection of a realistic condition for an unsteady LES simulation.

The grids were composed of 32 structured blocks in a stacked O-grid format. The cells were clustered towards the walls of the cylinder and the floor of the tunnel as shown in Figure 3(b). Table I shows the number of cells in each dimension around the cylinder. The numbers shown are the cell counts in the azimuthal and radial directions (N_c and N_r) and along the span of the cylinder (N_h). The cell sizes normal to the walls of the cylinder and the floor (S_r and S_h) and the azimuthal spacing (S_c) are also given. On the finest grid the near wall grid spacing on the floor of the tunnel was $0.002d$ and on the cylinder walls $0.0007d$ corresponding to y^+ values around 7. The grid topology and mesh are shown in Figure 3.

The time-step was set at 0.005 units, normalized with velocity and diameter, which corresponds to a CFL number of less than 1 in the high speed flow region at the side of the cylinder. The simulations were run until the flow reached a statistically steady state before starting to compute the turbulence statistics. It was found that 10 000 time-steps or 50 non-dimensional time units

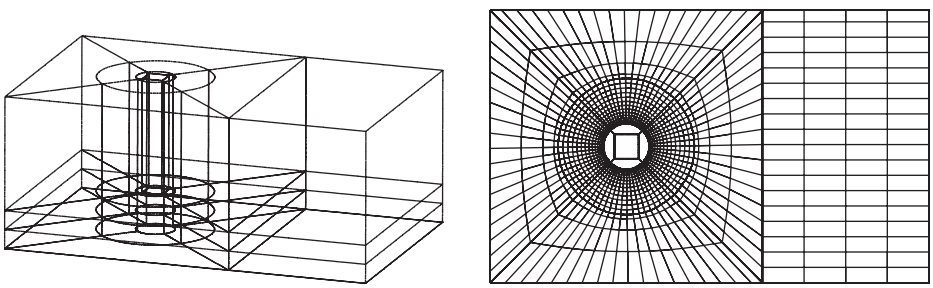

Figure 3. Diagrams showing grid structure and cell distribution: (a) arrangement of block structure; and (b) representation of the grid in the x-y plane (not all cells drawn).

Table I. Details of RANS/LES grids.

Grid no.	1	2	3
N_c	228	284	324
N_r	60	76	72
N_h	30	38	52
S_c	0.0138	0.0111	0.0098
S_r	0.0007	0.0007	0.002
S_h	0.002	0.002	0.002
Total cells	1 051 650	2 090 950	2 760 960

DOI: 10.1002/fld

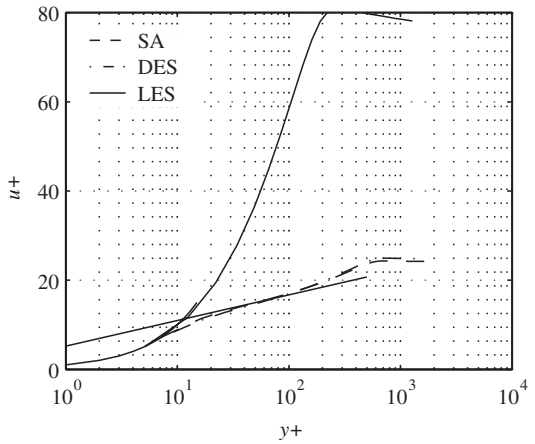

Figure 4. Flat plate boundary layer profiles for different models on the finest grid ($x/d = -0.5$).

was sufficient to reach the steady state after which a further 50 000 time-steps were run to obtain converged statistics. The simulations described here were run on a minimum of 6 dual-processor 1 GHz Pentium-III nodes and required approximately 1 min per time-step, which results in 1 week for 10 000 time steps. This calculation size was considered to be a practical upper limit for the computational resources available.

2.1. Assessment of boundary layer prediction

One of the key features of the truncated cylinder flow is the horseshoe vortex on the ground plane. The prediction of this is dependent on the oncoming boundary layer on the ground. It is therefore useful to assess the grid dependence of the boundary layer prediction for the models employed in this study. To do this a simple grid was constructed with the same length and height as the target model, that is $10.67d$ long by $4d$ high. For the RANS cases a two-dimensional grid was used, while for the LES and DES models a three-dimensional grid was employed with a z-dimension of $0.05d$. The cell sizes were chosen to be close to the grid used for the cylinder computations, with the minimum $y^+ = 7$ and $x^+ = z^+ = 18$. The grid was stretched in the x direction to match the actual model but with the cylinder removed so the smallest cells are at $x = 0$.

Normally when performing an LES simulation of a boundary layer one would use a fine enough grid in all dimensions to resolve the small-scale structures within the boundary layer. In the case of the cylinder on a ground plane however this would necessitate an excessively large number of cells. Therefore, the grid used will not be fine enough to resolve the boundary layer structures properly. However, it is of interest to know how the boundary profile will be affected by this. For the DES case the problem is not so severe as the model functions as a RANS model where the grid is stretched. However, there will be a region where the grid is refined around the base of the cylinder where the DES mode is activated. The effect of this is of interest while switching from RANS to LES mode.

The performance of the different models is compared in Figure 4. It can be seen that the SA and DES results are close, as expected, since the DES is functioning in RANS mode upstream of this point. The LES profile is more like a laminar boundary layer although the thickness is accurately

DOI: 10.1002/fld

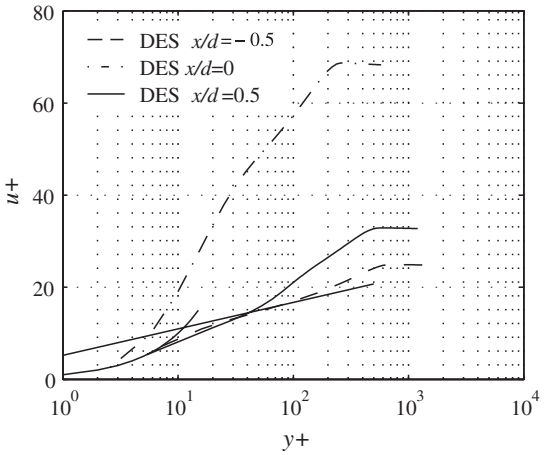

Figure 5. Flat plate boundary layer profiles at different x/d for the DES model on the finest grid.

predicted. This is because the grid is not fine enough to resolve the turbulent structures and the absence of wall-functions.

Figure 5 plots the boundary layer profiles of the DES model at different streamwise locations. The first curve at $x/d = -0.5$ is essentially the RANS solution. Beyond this point the grid is refined so that the model operates in LES mode. Here the turbulent viscosity is reduced due to the reduced length scale. If the Reynolds stresses were simulated correctly in this zone the velocity profile should remain correct. However, in this case the profile can be seen to straighten slightly. This suggests that the stresses are not being resolved fully. This is likely to be due to the lack of turbulent fluctuations entering this region from the RANS region upstream. This is an acknowledged weakness of DES and applies equally to areas of separation where the separated shear layer does not contain any turbulence from the boundary layer [7]. This effect can lead to grid-induced separation in boundary layers as shown by Menter [15].

The LES simulation fails to predict a fully turbulent boundary layer. This is to be expected as no wall model was used and the grid resolution was not fine enough to resolve the momentum carrying scales in the viscous sublayer. This defect is exaggerated by the stretching of the grid up and downstream of the cylinder location. Also no fluctuations are imposed at the inlet which will affect the accuracy of the LES model.

Figure 6 shows the streamwise variation in skin friction, C_f for the DES simulation. As the DES switching function is descending towards the wall as $x = 0$ is approached the cells get smaller. At some point, around $x/d = -0.75$ the LES part encroaches into the already established boundary layer (where $y+$ is of the order of a few hundred). At this point the resolved turbulence stresses have not had time to develop, but the modelled turbulent viscosity decays very quickly. In this region there is neither modelled nor resolved turbulence, hence the velocity gradient becomes shallower (more laminar) and the C_f reduces. Downstream the cell spacing expands again and the boundary layer is again modelled in RANS mode. This highlights the drawback of the simple approach to RANS/LES switching that during the transition from the RANS to DES the turbulence viscosity is not preserved as the destruction term is too severe for this region. The turbulent viscosity is transported into the LES regions and will damp out the desired fluctuations.

DOI: 10.1002/fld

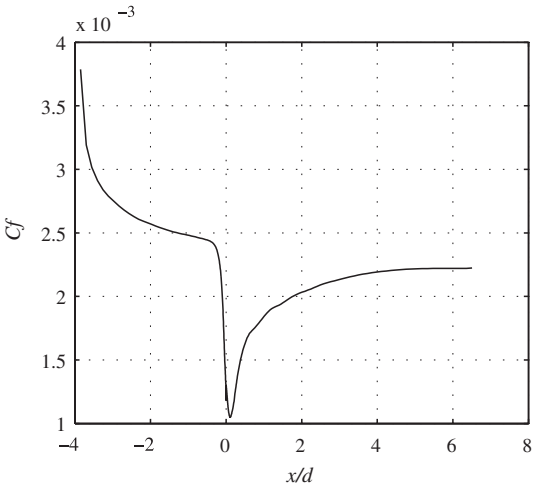

Figure 6. Variation of skin friction C_f with steamwise position x/d for DES.

Table II. Details of DES runs.

Model grid	LES 1	LES 2	DES 3	Exp.
Side separation, ϕ_s (deg)	83	81	84	70
Primary sep. from ground, X_{S1} (x/d)	−1.38	−1.45	−1.11	−1.0
Secondary sep. from ground, X_{S2} (x/d)	−1.00	−0.97	−0.98	−0.78
Attachment on free-end, X_{RT} (x/d)	0.30	0.39	0.41	0.17
Attachment on ground downstream, X_{RF} (x/d)	2.6	2.1	2.1	1.6
Base pressure coeff., C_{Pb}	0.63	0.62	0.45	0.58
Local C_D at $z/d = 0.5$	0.81	0.80	0.68	0.79

3. RESULTS AND DISCUSSION

3.1. Global flow parameters

The key parameters characterising the flow field for the two LES runs and the DES run are listed in Table II . The separation from the side of the cylinder occurs between 81 and 84° for all models. This is slightly surprising since the LES should produce laminar separation which occurs at 70° in the experiment. This could be due to poor boundary layer resolution on the cylinder surface. The separation points are close to 80° at which the flow separates when the boundary layer is tripped by a thin wire. This would be correct for the DES as the flow is assumed turbulent everywhere.

The extent of the primary horseshoe vortex, defined by the separation point, X_{S2}, on the ground plane upstream of the cylinder, is at $x/d = -1.0$ which is further forward than the measured position. The primary separation point X_{S1} is at $x/d = -1.38$ and -1.45 for the two LES grids and at $x/d = -1.11$ for the DES. It will be seen in the following section that the LES produces two large vortices, which cause these values to be so far upstream.

DOI: 10.1002/fld

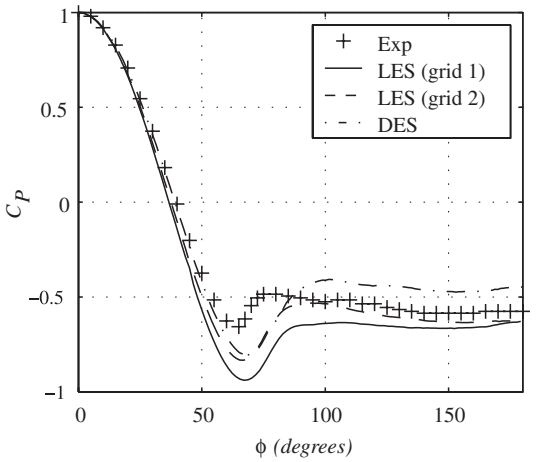

Figure 7. Plot of C_P around cylinder at $z/d = 0.5$.

The length of the recirculation region in the wake is characterized by the attachment point on the ground downstream of the body. This is predicted to be $x/d = 2.1$ by all the models. This point is further downstream than the experiments indicating a longer recirculation bubble.

The plots of the pressure coefficient, $C_P = (P - P_\infty)/(0.5\rho U_\infty^2)$, in Figure 7 show that the pressure on the surface of the cylinder is well predicted by all the simulations. The point of minimum C_P is close to the experimental one, while the local maximum or inflexion point just after separation is about 10° further back, corresponding to later separation. The base pressure is also close to the experimental value in the case of the LES. The DES has a higher base pressure. The similarity in the pressure distribution is reflected in the drag coefficient which is 0.79 in the experiment and 0.80 in the LES on the fine mesh. The DES gives a drag coefficient 15% lower due to the 30% higher base pressure.

3.2. Horseshoe vortex

The horseshoe vortex system extends too far forward in the LES simulations. This is reflected in the surface flow patterns in Figure 8(b) showing two separation lines in front of the cylinder and in Figure 9(b) in which a large pair of co-rotating vortices, along with a small counter-rotating vortex underneath, are evident upstream of the cylinder. While this topology is correct, the upstream vortex should be much thinner and not as long as predicted here. Indeed in the PIV measurements of this flow (Figure 9(a)) the upstream vortex is too close to the ground to be visible.

The failure to model this feature correctly is likely to be due to the poor resolution of the oncoming boundary layer. As seen in Figure 4 the boundary layer profile is closer to a laminar one which would cause a very different separation behaviour. In fact, according to Simpson [16], for a laminar boundary layer, the number of primary vortices increases with Re_d with two vortices, as seen here, occurring at $Re_d < 1000$ and three vortices above $Re_d = 1000$. As the number of vortices increases due to the instability of the system at higher Re_d it is likely that the present computations only give two vortices due to the extra viscosity and fuller boundary layer profile than the laminar case. The position of the upstream separation point is approximately $x/d = -1.7$ according to

DOI: 10.1002/fld

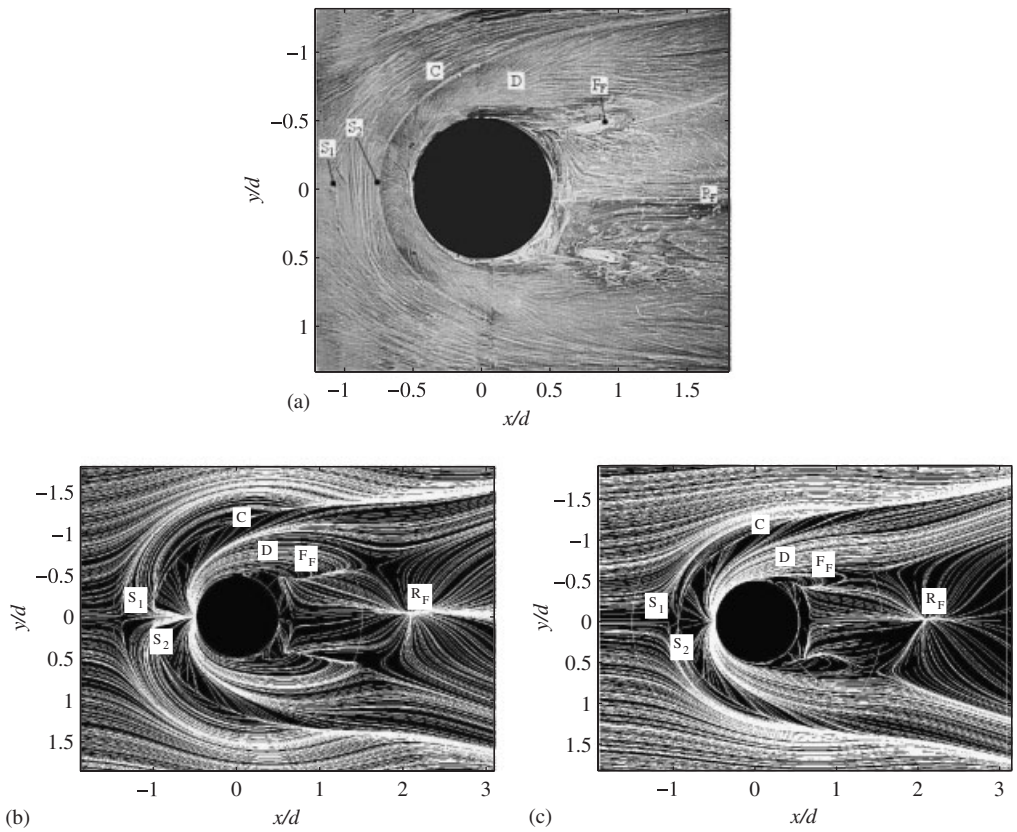

Figure 8. Surface flow visualization on the ground plane (flow from left to right): (a) experiment; (b) LES; and (c) DES.

Ballio *et al*. [17] at a Reynolds number based on displacement thickness of the boundary layer, Re_{δ^*}, of 409.

This failure of the LES model to capture the upstream flow correctly was one of the motivations for trying the DES method. As this would act as a RANS model in the boundary layer it could be expected to perform better than an earlier RANS simulation using the k–ε model [2]. The k–ε runs had shown very good agreement with the primary vortex although they did not capture the upstream vortex as it was too close to the wall. In practice, the DES simulation falls halfway between the LES and k–ε results. As shown by the primary separation position reported above the horseshoe vortex extends further forward than the one found in the experiment, but not as far as the LES one (cf. Figure 8(c)). In fact, the simulations do show a two vortex system as is expected with the primary separation close to the experimental position. The main vortex however is too far upstream with $X_{S2} = -0.98$ compared to $X_{S2} = -0.78$. The streamlines on the $y/d = 0$ plane, in Figure 9(c), show that the vortex centre is further forward, and the stagnation point on the cylinder wall appears to be lower than in the PIV measurements. These results are an

DOI: 10.1002/fld

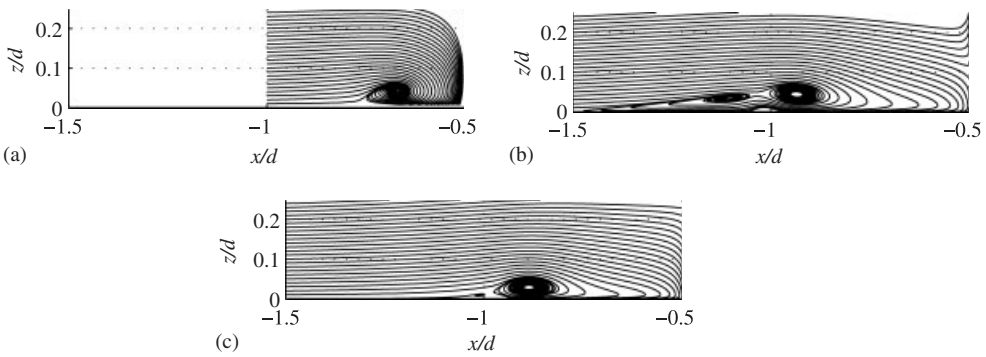

Figure 9. Streamlines on centreline ($y/d = 0$) upstream of cylinder: (a) experiment (PIV); (b) LES; and (c) DES.

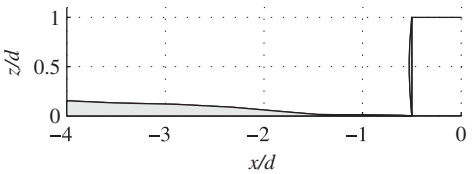

Figure 10. Upstream dividing line between RANS/LES for DES on $y/d = 0.0$.

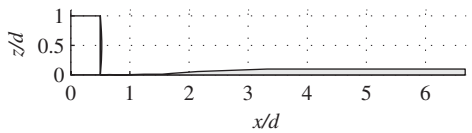

Figure 11. Upstream dividing line between RANS/LES for DES on $y/d = 0.0$.

improvement over both the LES and the k–ε model in terms of the secondary vortices but not as good as the RANS at predicting the primary vortex size and shape. This may be due to grid induced separation in the boundary layer upstream of the cylinder. However, it will also be influenced by the location of the DES switching descending into on-coming boundary layer as was found for the flat plate boundary layer. Figures 10 and 11 indicate the regions where the RANS is switched on and it can be seen in the region where the horseshoe vortex is located that there is likely to be some interaction.

The surface flow patterns in Figure 8 clearly show the separation line at the leading edge of the horseshoe vortex. The flow patterns, for both simulations, as the vortex trails downstream show similar features to the experimental image in terms of the flow directions under the vortex. The differences are caused by the excessive length of the upstream vortex.

DOI: 10.1002/fld

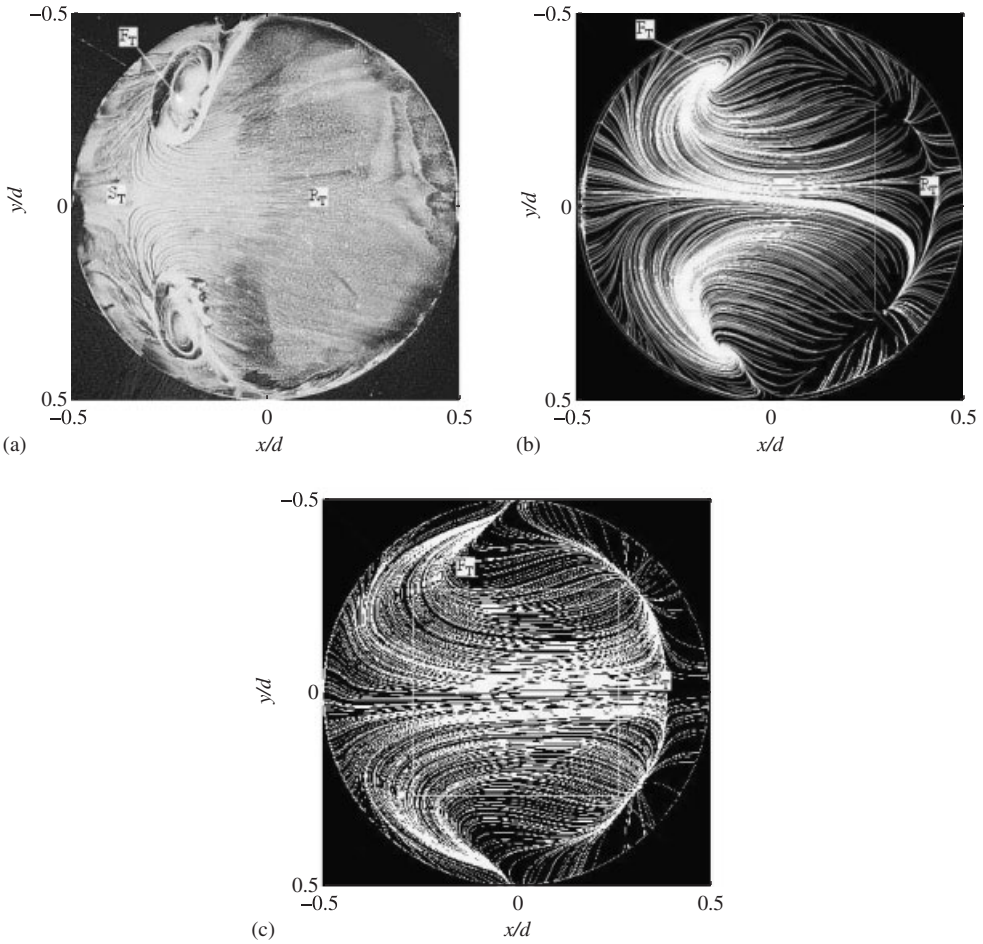

Figure 12. Surface flow visualization on the free-end of the cylinder (flow from left to right): (a) experiment; (b) LES; and (c) DES.

3.3. Flow over the free end

The two main features which characterize the flow above the free-end of the cylinder are the vertical and streamwise extents of the recirculation bubble and the swirl patterns on the surface of the tip. Comparing the surface flow pattern in Figure 12, obtained from the LES simulation on grid 2, with the image from the experiment, it can be seen that the swirl patterns are similar. The location of the vortex core is in the same position although it is difficult to judge from the experiment due to the accumulation of oil at this spot. Three saddle points can be seen towards the rear of the cylinder along the attachment line. The location of this line is not clear on the experimental picture. In the experiment there appears to be flow from the leading edge moving back as far as a separation point at $x/d \sim -0.4$, which must be due to a small vortex in front of

DOI: 10.1002/fld

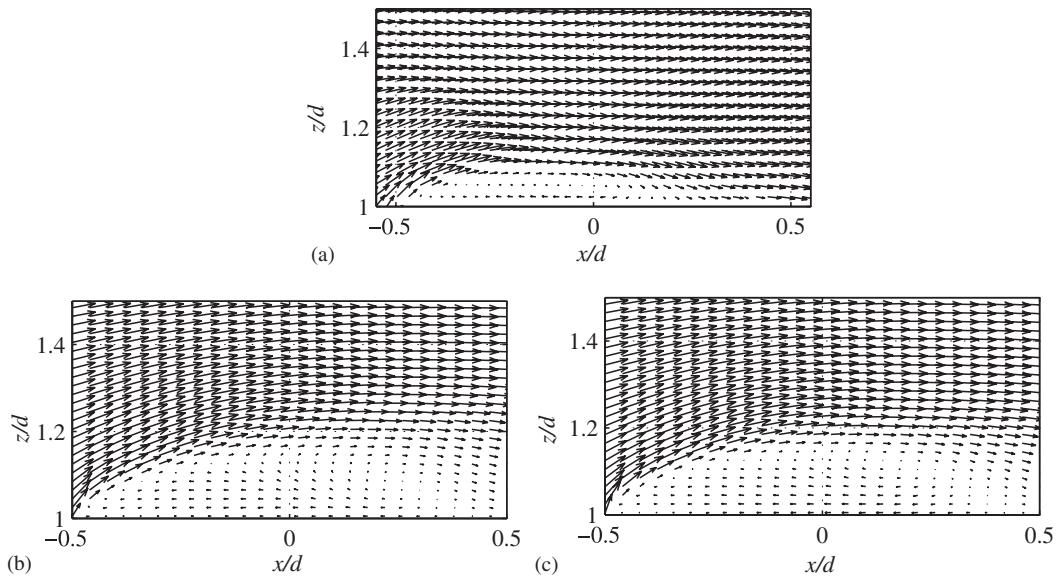

Figure 13. Velocity vectors on centreline ($y/d = 0$) on top cylinder: (a) experiment (PIV); (b) LES; and (c) DES.

and beneath the main recirculation. This does not appear in the LES results where all the flow is from the back of the cylinder.

In the case of the DES simulations the swirl patterns are not completely captured, although the direction of the streaklines is correct. It is just the wrapping up of the vortex eye which is not resolved. The prediction of this flow feature is likely to depend strongly on the ability of the model to predict the boundary layer flow on the top surface of the cylinder. Due to the low speeds and strong pressure gradients in this region the nature of this boundary layer may be difficult to predict using RANS type models.

The flow pattern in the $y/d = 0$ plane (Figure 13) shows that the recirculation vortex predicted by the simulations is much larger than that measured by the PIV. The centre is further downstream, resulting in a later attachment to the free-end. Attachment occurs at $x/d = 0.39$ in the LES (grid 2) and at $x/d = 0.41$ in the DES both of which are further back than the experimental value of $x/d = 0.17$. The centre of the vortex is located at $x/d = 0.3$ in the LES compared to $x/d = 0$ in the experiment. The coarser grid gives a shorter recirculation bubble than the finer mesh with attachment at $x/d = 0.3$.

Figure 14 which plots U against z/d at $x/d = 0$ shows that the peak velocity in the LES (grid 2) and DES simulations occurs 60% higher than in the experiment. The velocity profile close to the surface of the cylinder is close to the experimental points in the fine mesh LES with the correct maximum backflow velocity. In the DES the flow near the surface is faster with a thinner boundary layer. The overprediction of the size of this vortex may be due to the uniform flow inlet boundary condition with no imposed turbulence.

There has been some debate over the topology of the flow over the free-end [18, 19]. This is one area in which the experimental data gathered so far does not fully identify the flow behaviour

DOI: 10.1002/fld

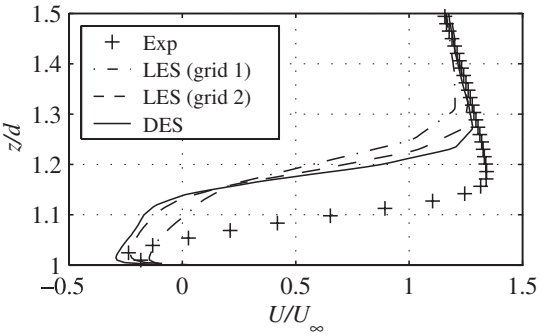

Figure 14. Plot of streamwise velocity against z/d at $x/d = 0$.

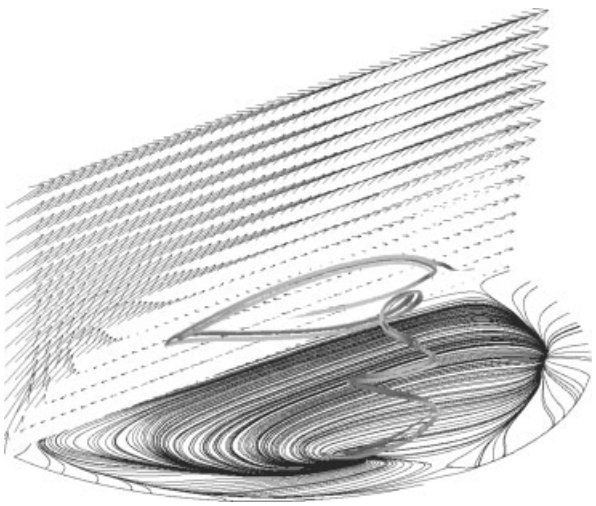

Figure 15. Mean flow over the free-end of the cylinder from DES results. Velocity vectors shown on centreplane, surface flow streaklines on the cylinder top surface and particle paths showing motion of particles from the vortex eye on the surface.

due to its strong three dimensionality. The numerical simulations however provide a complete picture of the flow topology. This is shown in Figure 15 which shows vectors in the centreplane and on the free-end along with particle paths connecting the two. The particle traces show that the vortex formed in the centreplane recirculation region is connected to the two eyes on the top of the cylinder by a vortex structure. This supports the hypothesis of Kawamura *et al*. [19] of the mushroom vortex. This demonstrates the merit of doing numerical simulations to enable better understanding of experimental data.

DOI: 10.1002/fld

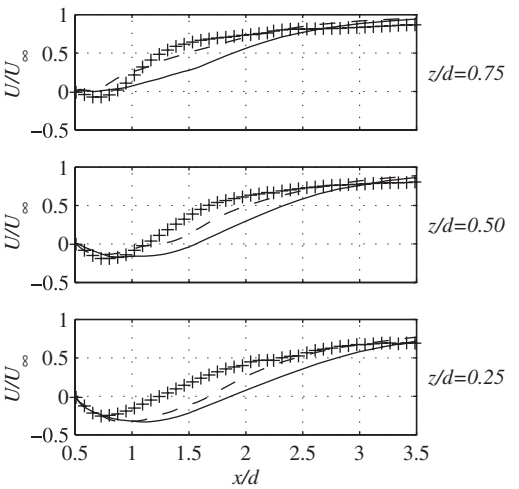

Figure 16. Comparison of U-velocity distribution along centreline in wake.
+ PIV measurements, — LES, – – DES.

3.4. Wake region

As previously stated the separation length in the wake is overpredicted by all the simulations, with attachment at $x/d = 2.1$. This can be related to the oversize recirculation region above the free-end which pushes the shear layer up. Figure 16 shows U against z/d for different heights above the ground. This shows that the backflow velocity is quite close to the experimental values, but that the streamwise extent of the reversed flow is too long. The velocity recovery downstream is slower than in the experiments. The DES results are generally closer to the experiment than the LES, particularly in the upper half of the wake.

More detail of the structure of the wake can be seen in Figures 17 and 18. Figure 17 shows profiles of U, W and k against z/d at different locations along the centreline. The data is compared to the PIV measurements. The normal stresses $u_i u_i$ are plotted in Figure 18. k here represents the resolved turbulent kinetic energy, as the modelled energy was found to be significantly smaller than the resolved.

The U velocity profiles show the effect of the higher shear layer with the peak velocity being higher than in the experiment. The DES is closer than the LES, particularly downstream beyond reattachment where the agreement is very good. The W profiles show a similar picture with the DES being close to the measured values while the LES gives lower downwash velocities. This is likely to be due to the shape of the shear layer being more horizontal behind the cylinder. Both results tend to agree better further downstream where the flow is dominated by a streamwise vortex pair, which is well predicted by all models.

The resolved turbulent kinetic energy, k, is quite well simulated although it is slightly high in the shear layer. This is mirrored in the profiles of $u'u'$ which are overpredicted in the shear layer. $v'v'$ is generally underpredicted and does not follow the shape of the profile at all. $w'w'$ is closer to the experiment although the difference in the position of the shear layer affects the profile.

DOI: 10.1002/fld

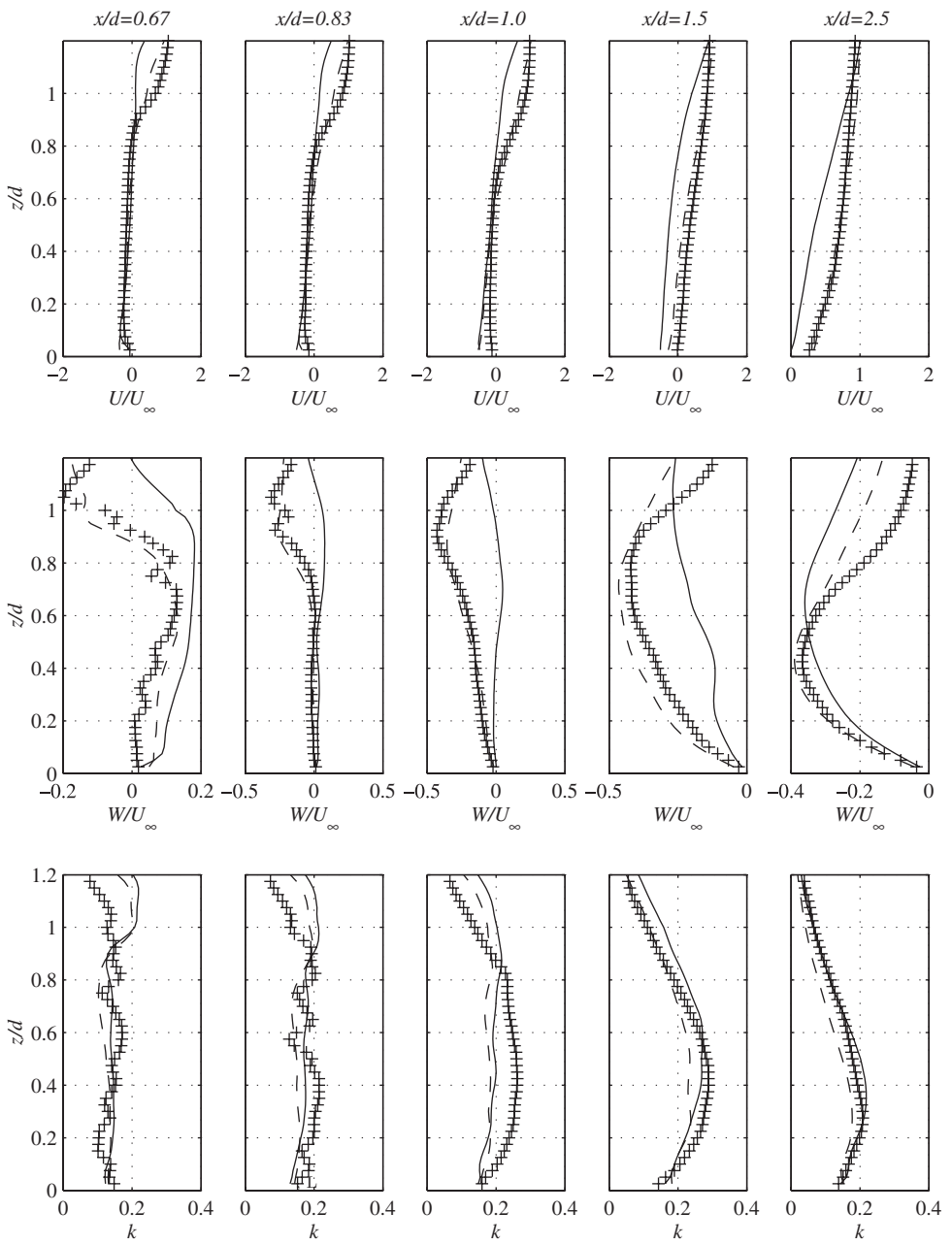

Figure 17. Profiles of velocity and turbulent kinetic energy at $y/d = 0$ in wake region. + PIV measurements, — LES, – – DES.

DOI: 10.1002/fld

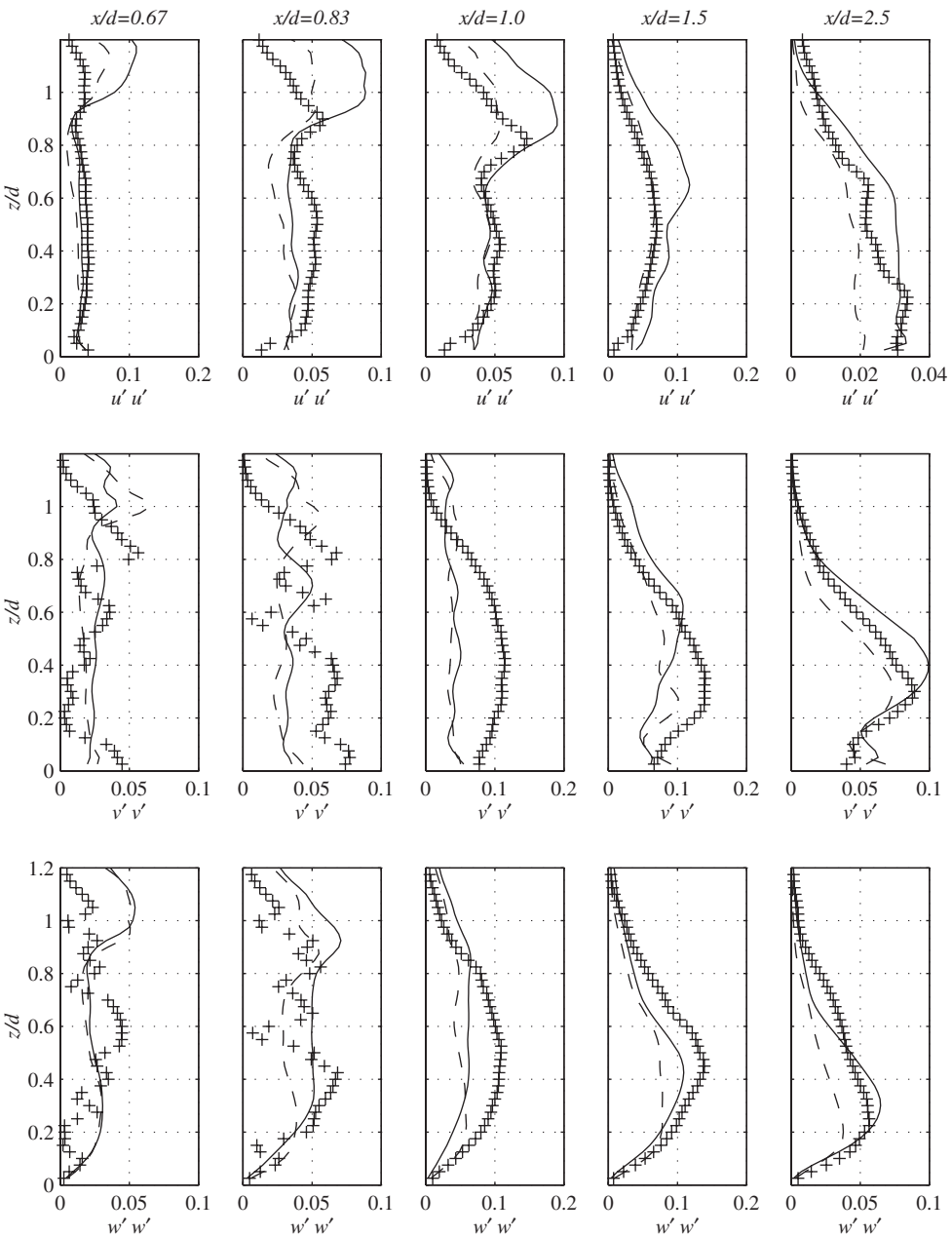

Figure 18. Profiles of normal stresses at $y/d = 0$ in wake region. + PIV measurements, — LES, – – DES.

The overall pattern of the flow can be seen in the vector plots in Figure 19. These show reasonable agreement particularly downstream where the large streamwise vortices have formed. The tip vortices off the free-end are captured.

DOI: 10.1002/fld

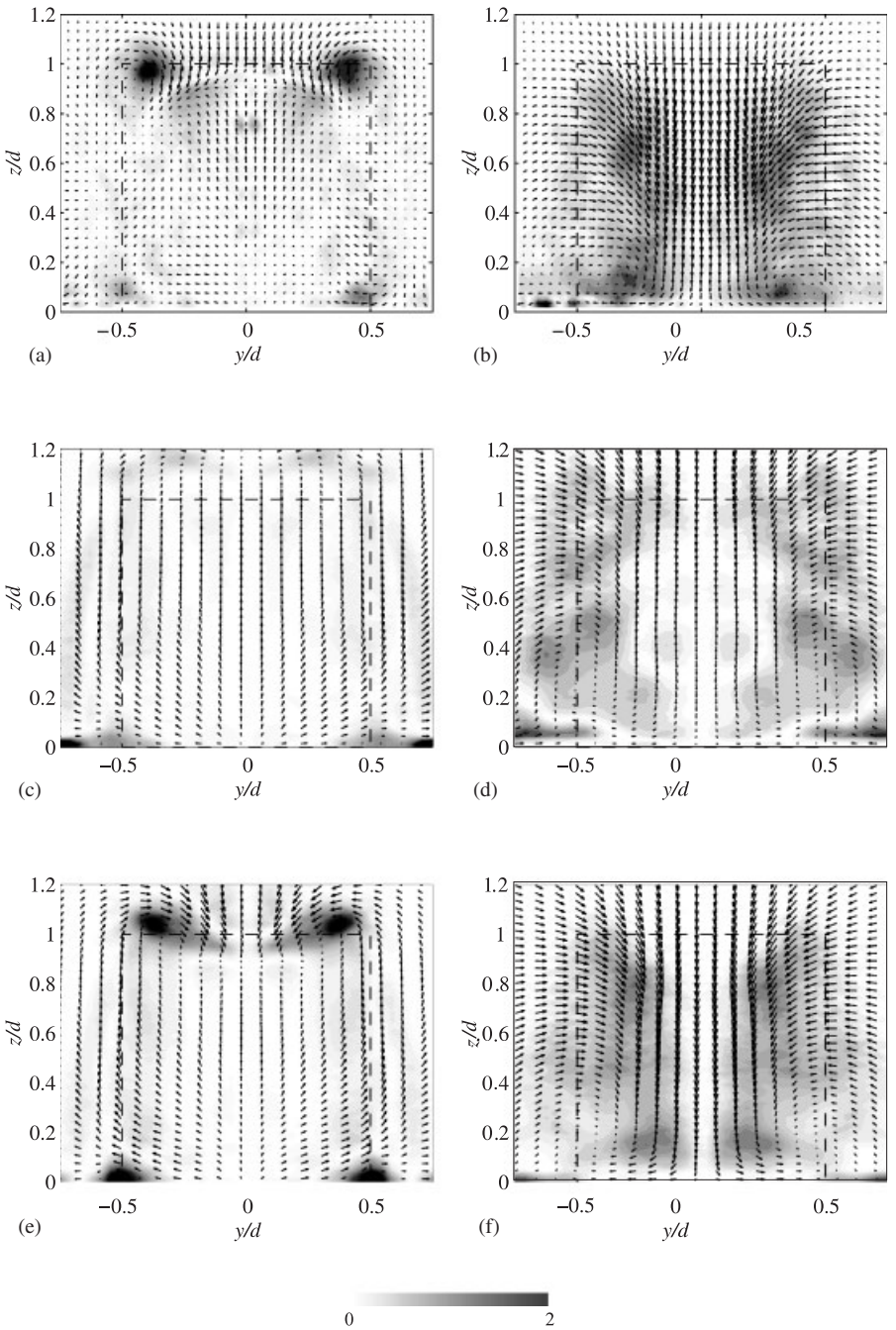

Figure 19. Velocity vectors and vorticity contours: (a) $x/d = 0.67$ (PIV); (b) $x/d = 1.5$ (PIV); (c) $x/d = 0.67$ (LES); (d) $x/d = 1.5$ (LES); (e) $x/d = 0.67$ (DES); and (f) $x/d = 1.5$ (DES).

DOI: 10.1002/fld

4. CONCLUSIONS

LES and DES simulations of the flow around a low aspect-ratio cylinder on a ground plane have been performed and compared against PIV measurements.

The flow on the surface of the free-end in the LES was found to agree well with the experiments as the boundary layer on this surface was correctly resolved. The shear layer above the free-end was too high with the attachment point being 33% too far back. The DES also predicted the correct flow patterns although the swirl pattern was not as clear. The size of the recirculation bubble was similar to the LES. The numerical simulations resolve a previous debate—as to the correct free-end flow topology that is difficult to obtain experimentally—in favour of the work of Kawamura *et al*. [19].

Overall, the DES showed better agreement with the experimental data than the LES (particularly in terms of velocity profiles). However, in general, the turbulent kinetic energy and the normal stresses compared equally favourably with experiment in both the LES and the DES.

The main failing of the LES simulation was in the prediction of the boundary layer on the ground plane upstream of the cylinder. This was due to the known lack of grid resolution for fully resolving the turbulence scales in the boundary layer, and the lack of a wall function. This led to an incorrect modelling of the horseshoe vortex with the upstream vortex being too large. The separation point in front of the first vortex was over three times further upstream than the experimental measurement. The DES method was tested to try to overcome this failing. The boundary layer upstream was modelled correctly but the primary separation from the ground 22% further upstream and the secondary separation was 71% too far upstream. This is likely to be due to the transition from RANS to DES mode in this region. Despite these shortcomings, this work demonstrates the ability of both LES and DES to capture complex, unsteady flow around a bluff body representative of many practical applications. It is evident that greater mesh resolution is required in LES and further work is required when using DES to improve the coupling between the frozen RANS and unsteady LES zones. However, due to the significant computational expense associated with finely resolved LES meshes, improvements in the DES model is to be recommended for unsteady simulations of practical problems.

ACKNOWLEDGEMENTS

The work described in this paper was supported by a PhD studentship from the School of Engineering Sciences, University of Southampton.

REFERENCES

1. Pattenden RJ, Turnock SR, Zhang X. Measurements of the flow over a low aspect-ratio cylinder mounted on a ground plane. *Experiments in Fluids* 2005; **39**:10–21.
2. Pattenden RJ. An investigation of the flow around a truncated cylinder. *Ph.D. Thesis*, University of Southampton, 2004.
3. Baker CJ. The turbulent horseshoe vortex. *Journal of Wind Engineering and Industrial Aerodynamics* 1980; **6**:9–23.
4. Pattenden RJ, Turnock SR, Bressloff NW. An experimental and computational study of three-dimensional unsteady flow features found behind a truncated cylinder. *24th Symposium on Naval Hydrodynamics*, Fukuoka, Japan, 2002.
5. Fröhlich J, Rodi W. LES of the flow around a circular cylinder of finite height. *International Journal of Heat and Fluid Flow* 2004; **25**(3):537–548.

DOI: 10.1002/fld

6. Kappler M. Experimentelle Untersuchung der Umströmung von Kreiszylinder mit ausgeprägt dreidimensionalen Effekten. *Ph.D. Thesis*, Institute for Hydromechanics, University of Karlsruhe, 2002.
7. Travin A, Shur M, Strelets M, Spalart P. Detached-eddy simulations past a circular cylinder. *Flow*, *Turbulence and Combustion* 2000; **63**:293–313.
8. Bressloff NW. A parallel pressure implicit splitting of operators algorithm applied to flow at all speeds. *International Journal for Numerical Methods in Fluids* 2001; **36**:497–518.
9. Van Leer B. Towards the ultimate conservative difference scheme. II. Monotonicity and conservation combined in a second order scheme. *Journal of Computational Physics* 1974; **14**:361–370.
10. Métais O, Lesieur M. Spectral large-eddy simulations of isotropic and stably-stratified turbulence. *Journal of Fluid Mechanics* 1992; **239**:157–194.
11. Piomelli U, Balaras E. Wall-layer models for large-eddy simulations. *Annual Review of Fluid Mechanics* 2002; **34**:349–374.
12. Spalart PR, Jou W-H, Strelets M, Allmaras SR. Comments on the feasibility of LES for wings, and on a hybrid RANS/LES approach. *Advances in DNS/LES*, *1st AFOSR International Conference on DNS/LES*. Greyden Press: Columbus, OH, 1997.
13. Spalart PR, Allmaras SR. A one-equation turbulence model for aerodynamic flows. *La Recherche Aérospatiale* 1994; **1**:5–21.
14. Shur M, Spalart PR, Strelets M, Travin A. Detached-eddy simulation of an airfoil at high angle of attack. *4th International Symposium on Engineering Turbulence Modelling and Measurements*, 1999.
15. Menter F, Kuntz M, Langtry R. Ten years of industrial experience with the SST turbulence model. In *Turbulence*, *Heat and Mass Transfer*, Hanjalic K, Nagano Y, Tummers M (eds), vol. 4. Begell House Inc.: New York, 2003.
16. Simpson RL. Junction flows. *Annual Review of Fluid Mechanics* 2001; **33**:415–443.
17. Ballio F, Bettoni C, Franzetti S. A survey of time-averaged characteristics of laminar and turbulent horseshoe vortices. *Transactions on ASME*, *Journal of Fluids Engineering* 1998; **120**:233–242.
18. Roh SC, Park SO. Vortical flow over the free end surface of a finite circular cylinder mounted on a flat plate. *Experiments in Fluids* 2003; **34**:63–67.
19. Kawamura T, Hiwada M, Hibino T, Mabuchi I, Kumuda M. Cylinder height greater than turbulent boundary layer thickness—flow around a finite circular cylinder on a flat plate. *Bulletin of the JSME* 1984; **27**(232):2142–2151.

DOI: 10.1002/fld